ssDNA is an allosteric regulator of the *C. crescentus* SOS-independent DNA damage response transcription activator, DriD

Kevin Gozzi,[1] Raul Salinas,[2] Viet D. Nguyen,[2] Michael T. Laub,[1,3] and Maria A. Schumacher[2]

[1]Department of Biology, Massachusetts Institute of Technology. Cambridge, Massachusetts 02139, USA; [2]Department of Biochemistry, Duke University Medical Center, Durham, North Carolina 27710, USA; [3]Howard Hughes Medical Institute, Massachusetts Institute of Technology, Cambridge, Massachusetts 02139, USA

DNA damage repair systems are critical for genomic integrity. However, they must be coordinated with DNA replication and cell division to ensure accurate genomic transmission. In most bacteria, this coordination is mediated by the SOS response through LexA, which triggers a halt in cell division until repair is completed. Recently, an SOS-independent damage response system was revealed in *Caulobacter crescentus*. This pathway is controlled by the transcription activator, DriD, but how DriD senses and signals DNA damage is unknown. To address this question, we performed biochemical, cellular, and structural studies. We show that DriD binds a specific promoter DNA site via its N-terminal HTH domain to activate transcription of genes, including the cell division inhibitor *didA*. A structure of the C-terminal portion of DriD revealed a WYL motif domain linked to a WCX dimerization domain. Strikingly, we found that DriD binds ssDNA between the WYL and WCX domains. Comparison of apo and ssDNA-bound DriD structures reveals that ssDNA binding orders and orients the DriD domains, indicating a mechanism for ssDNA-mediated operator DNA binding activation. Biochemical and in vivo studies support the structural model. Our data thus reveal the molecular mechanism underpinning an SOS-independent DNA damage repair pathway.

[*Keywords*: *Caulobacter crescentus*; DNA repair; DriD; WYL motif; ssDNA; transcriptional activator]

Supplemental material is available for this article.

Received March 7, 2022; revised version accepted May 12, 2022.

The maintenance of genomic integrity is essential for all life, yet cells are exposed to a myriad of environmental and metabolic assaults that inevitably lead to DNA mutation and damage. To counter such episodes, organisms have evolved DNA damage response systems that transiently halt the cell cycle to prevent cell division until the damage can be resolved (Hartwell and Weinert 1989; Harper and Elledge 2007). Indeed, tight coordination between the DNA damage response and cell division is required to prevent genomic instability. The best-characterized DNA damage response system in bacteria is the SOS pathway, which was originally discovered in *Escherichia coli* (Little and Mount 1982; Jaffé et al. 1986; Erill et al. 2007). In this system, DNA damage is sensed by the presence of single-stranded DNA (ssDNA) that binds RecA. The interaction between RecA and ssDNA leads to the formation of RecA filaments, which trigger the autocatalytic cleavage of LexA (Little et al. 1980; Phizicky and Roberts 1981; Galletto et al. 2006). In *E. coli*, cleavage and inactivation of LexA allows the transcription of DNA repair genes and the cell division inhibitor *sulA* (Huisan and D'Ari 1981; Mukherjee et al. 1998; Opperman et al. 1999). SulA binds directly to FtsZ, disrupting FtsZ polymerization, thus preventing Z ring formation and halting cell division until DNA damage is repaired (Mukherjee et al. 1998; Trusca et al. 1998). However, SulA is not widely conserved beyond the γ-proteobacteria, and recent work has demonstrated that additional SOS-induced division inhibitors exist in a range of bacteria (Dullaghan et al. 2002; Kawai et al. 2003; Chauhan et al. 2006; Ogino et al. 2008; Modell et al. 2011).

Caulobacter crescentus serves as an excellent model system for understanding the DNA damage response

Corresponding authors: maria.schumacher@duke.edu, laub@mit.edu
Article published online ahead of print. Article and publication date are online at http://www.genesdev.org/cgi/doi/10.1101/gad.349541.122. Freely available online through the *Genes & Development* Open Access option.

and its coordination with the bacterial cell cycle because these bacteria are easily synchronized and DNA replication initiates only once per cell division. In *C. crescentus* the SOS-induced inhibitor was identified as SidA, which functions not by binding directly to FtsZ, as with SulA, but by forming a complex with FtsW, a divisome protein that assembles at the later stages of cytokinesis (Modell et al. 2011). Although SOS-dependent regulators, such as SidA and SulA, have been thought to be the primary or only mechanism for inhibiting cell division after DNA damage, recent studies have indicated the existence of SOS-independent division regulation systems. For example, experiments in *Bacillus subtilis*, *E. coli*, and *C. crescentus* have shown that cells that lack SOS-induced inhibitors or cells that have been rendered unable to generate an SOS response still become filamentous following a DNA damage event, suggesting other mechanisms exist to block cell division (Howe and Mount 1975; Huisman et al. 1980; Huisman and D'Ari 1981; Hill et al. 1997; Liu et al. 2001). In particular, although SidA is the main SOS-dependent division inhibitor in *C. crescentus*, cells that lack *sidA* were shown to be capable of cell division arrest when exposed to the DNA-damaging agent mitomycin C (Modell et al. 2014). Subsequent experiments revealed the presence of DidA as the first damage-induced, SOS-independent division regulator in *C. crescentus* (Modell et al. 2014).

Overexpression of *didA* in undamaged cells is sufficient to inhibit cell division in *C. crescentus* (Modell et al. 2014). The target of DidA is another late arriving divisome component, FtsN, which forms a complex with FtsW and FtsI, and is important for triggering cell division. The interaction with DidA appears to impair the activity of this complex (Modell et al. 2014). DidA expression is barely detectable during normal cell growth, with DNA damage required to activate transcription of the *didA* gene. Genetic screens to identify factors important in *didA* expression uncovered the gene CCNA_01151 as essential for *didA* expression (Modell et al. 2014). CCNA_01151 encodes a putative DNA binding protein of the DeoR family of regulators. Hence, the protein was called DriD (for DeoR inducer of *didA*).

DriD is a 327-residue protein that contains a putative WYL (named for a conserved Trp–Tyr–Leu sequence) motif. The WYL domain, although poorly understood, is found in a wide array of proteins and is enriched near CRISPR cassettes and associated Cas genes (Makarova et al. 2014). To date, few structures of WYL-containing proteins have been reported. However, bioinformatic analyses indicate that WYL domains are most often fused to an N-terminal HTH domain and may bear additional fusions to domains with enzymatic functions, including endonuclease, exonuclease, helicase, and nucleotidyl transferase activity. Indeed, the N-terminal region of DriD is predicted to contain a HTH motif. Consistent with a role for DriD in DNA binding, data indicated that it functions as a transcriptional activator of *didA* expression. Importantly, a prior study showed that DriD levels remained the same during the cell cycle, indicating that changes in DriD expression are not what drives *didA* activation (Modell et al. 2014). In particular, while DriD protein levels remain the same during the *C. crescentus* cell cycle, the occupancy of DriD at the P_{didA} promoter increased significantly following DNA damage, indicating that DriD activity is post-translationally regulated. However, what DNA damage signals are recognized by DriD and how these signals impact the transcription activity of DriD remain unknown.

To gain insight into these questions, we performed cellular, biochemical, and structural studies on the *C. crescentus* DriD protein. Strikingly, we found that ssDNA binds the DriD C-terminal region, which contains a WYL domain and WYL C-terminal extension (WCX) dimerization domain. Structures of apo and DriD–ssDNA complexes show that ssDNA binding leads to stabilization and reorientation of the WYL domain to which the HTH domain is attached. Biochemical and cellular studies show that ssDNA binding to DriD stimulates its ability to bind operator DNA and also the ability of DriD to activate transcription. Collectively, these studies reveal the molecular basis for the activation of this SOS-independent DNA repair pathway.

Results

Identification of the DriD consensus binding site

Previous studies showed that DriD binds to the *didA* promoter upon cellular DNA damage (Modell et al. 2014). To begin to delineate the specific DriD binding site within the *didA* promoter, we recombinantly expressed and purified full-length (FL) DriD from *C. crescentus* with an additional C-terminal His_6 tag and performed electrophoretic mobility shift assays (EMSAs) with linear dsDNA corresponding to the *didA* promoter. Incubation of an increasing concentration of DriD-His_6 resulted in a shift of the 300-bp *didA* promoter DNA, indicative of promoter–DriD complex formation (Fig. 1A). As a control, we tested binding of DriD to an intragenic region of *ruvA*, a gene upregulated during the canonical SOS DNA damage response, which demonstrated much weaker binding than the *didA* promoter. Quantification of DriD-His_6 binding curves revealed an apparent K_d of ~65.9 nM for the *didA* promoter and ~352.3 nM for the *ruvA* gene (Supplemental Fig. S1). To further narrow down the region of the *didA* promoter sufficient for binding of DriD-His_6, we performed EMSAs on three fragments spanning the *didA* promoter (Fig. 1B) and found that only the fragment containing the predicted −10 and −35 regions exhibited strong binding by DriD-His_6 (Fig. 1B). We then tested 40-bp sections of this fragment and observed binding of DriD-His_6 to the two fragments spanning −73 to −34 and −53 to −14, relative to the start codon (Fig. 1C, fragments B and C). Given that binding of DriD-His_6 to the −73 to −34 fragment was slightly stronger than the binding to the −53 to −14 fragment, we then tested 20-bp fragments that shifted every 4 bp along the −73 to −34 fragment, finding the strongest binding of DriD-His_6 to the −57 to −38 fragment with an affinity comparable with that of DriD-His_6 binding to the full-length promoter

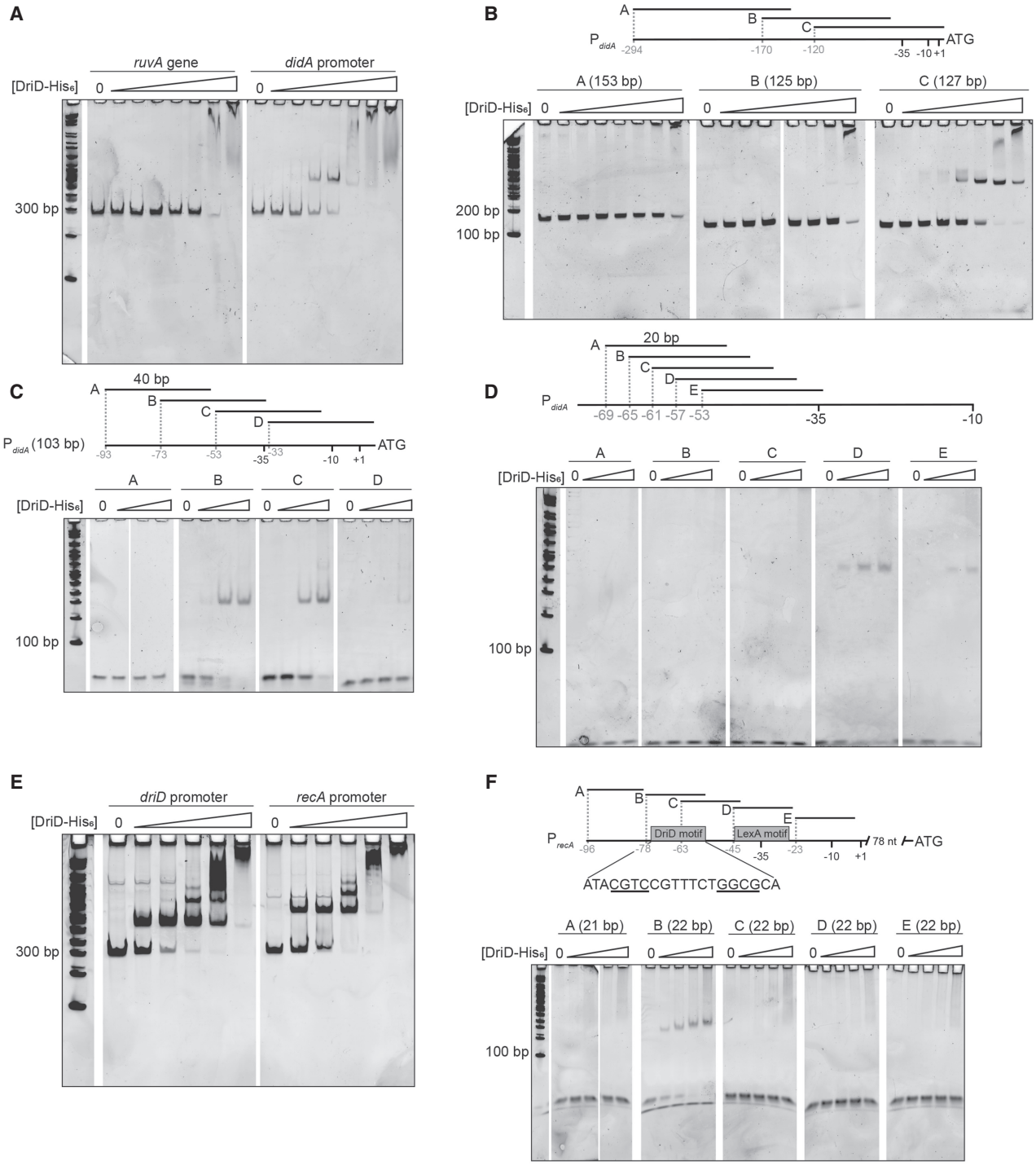

Figure 1. DriD-His$_6$ binds a defined motif in several promoters. (*A*) Electrophoretic mobility shift assays (EMSAs) of increasing concentrations (0, 15.6, 31.3, 62.5, 125, 250, 500, and 1000 nM) of purified DriD bearing a C-terminal His$_6$ tag (DriD-His$_6$) incubated with 300-bp region of a control intragenic region (in *ruvA*) and with the 300-bp promoter of *didA*. (*B*) EMSAs of increasing concentrations (0, 15.6, 31.3, 62.5, 125, 250, 500, and 1000 nM) of DriD-His$_6$ with three ~140-bp regions spanning the 300-bp *didA* promoter. Fragments A–C overlap as shown. (*C*) EMSAs of increasing concentrations (0, 31.3, 125, and 250 nM) of DriD-His$_6$ with four 40-bp regions spanning the 100 bp upstream of the *didA* start codon. Fragments A–D overlap as shown. (*D*) EMSAs of increasing concentrations (0, 31.3, 125, and 250 nM) of DriD-His$_6$ with five nested 20-bp regions spanning the –80- to –41-bp fragment upstream of the *didA* start codon. Fragments A–E overlap as shown. (*E*) EMSAs of increasing concentrations (0, 31.3, 62.5, 125, 250, and 500 nM) of DriD-His$_6$ with the *driD* and *recA* promoters. The putative DriD binding site is shown, with inverted repeats underlined. (*F*) EMSAs of increasing concentrations (0, 15.6, 31.3, 62.5, and 125 nM) of DriD-His$_6$ with five 20-bp regions spanning the 100 bp upstream of the *recA* start codon. Fragments A–E overlap as shown, with fragment B spanning the putative DriD binding motif.

(Fig. 1D, fragment D). These analyses revealed a minimal 20-bp dsDNA site, ATACGTCCGTTTCTGGCGCA, that was sufficient for DriD-His_6 binding, as only DNA fragments containing some or all of this sequence exhibited binding (Fig. 1A–D). The 3′ end of this motif is at position −36 relative to the putative +1 site, 1 nt upstream of the −35 site (Supplemental Fig. S2A–C). As EMSA studies were performed with a C-terminally His-tagged DriD, we carried out in vivo analyses to assess whether the presence of the C-terminal His_6 tag impacted DriD function. These experiments showed that the C-terminally His-tagged variant of DriD can complement a *driD* deletion strain similar to the untagged version (Supplemental Fig. S2D).

DriD binds driD *and* recA *promoters*

We searched the *C. crescentus* NA1000 genome for additional DriD binding sites by looking for matches to the 20-bp binding site identified within the *didA* promoter, allowing up to three mismatches across the motif. We found two additional occurrences of the motif across the genome: one in the promoter of *driD* itself with two mismatches and one in the *recA* promoter with three mismatches. *recA* encodes the cell's primary recombinase, which mediates recombination and activation of the canonical SOS response (Galhardo et al. 2005; da Rocha et al. 2008). To determine whether DriD binds these other promoters, we performed EMSAs with *driD* and *recA* promoter DNA (Fig. 1E). These experiments revealed that DriD indeed binds both promoters with high (nanomolar [nM]) affinity (28.2 and 21.4 nM, respectively), similar to that seen with the *didA* promoter. By performing EMSAs with sections of the *recA* promoter, we found that only the portion of the promoter containing the putative DriD motif produced a shift when incubated with DriD-His_6 (Fig. 1F). The *recA* promoter contains a binding site for LexA, the SOS response repressor, that straddles the −35 site of the promoter, occluding binding of RNA polymerase (RNAP) and preventing transcription activation (da Rocha et al. 2008).

The 3′ end of the DriD binding motif is 17 nt upstream of the −35 box, putting DriD in a favorable position to act as a potential transcriptional activator by recruiting the RNAP holoenzyme. The +1 site of the *driD* transcript has not been well characterized, given that it is typically expressed at low levels in the absence of damage when most global analyses have been done (Zhou et al. 2015). At the *driD* promoter, the 3′ end of the 20-bp motif is 10 nt upstream of the predicted start codon, suggesting that DriD may negatively autoregulate its own expression. Diagrams of the orientation of the motif to regions in the respective promoters are shown (Supplemental Fig. S2A). Further searches for putative DriD binding motifs with additional mismatches revealed motifs in several other promoters across the genome, including *recJ* (ssDNA exonuclease), *dnaG* (DNA primase), and *bapE* (a nuclease), shown relative to their predicted transcription start sites (Supplemental Fig. S2A).

ChIP analyses of DriD binding

To determine whether DriD binds other genes across the genome, we performed chromatin immunoprecipitation (ChIP) on cells bearing a C-terminal FLAG-tagged DriD (DriD-3xFLAG). Samples were harvested both following global double-strand break (DSB) DNA damage induced by addition of the bleomycin derivative zeocin and following a single DSB by using a strain engineered with an inducible restriction enzyme (I-SceI) and a corresponding restriction site encoded on the genome (Fig. 2A; Badrinarayanan et al. 2015). To verify that DriD-3xFLAG localizes to the known target, *didA*, we harvested samples after damage induction and isolated DriD-3xFLAG-bound DNA fragments by immunoprecipitation with quantitative PCR (qPCR). We observed an approximately fourfold enrichment of the *didA* promoter in the ChIP sample compared with the input control from zeocin-treated samples, and an approximately fivefold enrichment in the single-DSB strain, with no enrichment in uninduced strains or in cells containing only the native untagged version of DriD (Fig. 2B). Each treatment condition, DriD-3xFLAG with zeocin or DriD-3xFLAG and P_{van}-*i-sceI* with vanillate, had a respective negative control condition for internal comparison (no zeocin or no vanillate, respectively). The untagged WT DriD condition was also included to highlight any spurious binding of the anti-FLAG beads that may be consistent across all samples. We then paired ChIP with deep sequencing (ChIP-seq) to determine global occupancy of DriD during DNA-damaging conditions. As expected, we saw strong enrichment of DriD-3xFLAG at the *didA* promoter both during a single-DSB and zeocin treatment, and no enrichment was seen in the absence of damage or in a strain with an untagged DriD (Fig. 2C). Across the rest of the genome, we saw enrichment of DriD-3xFLAG following zeocin treatment in promoter regions for *driD*, *recA*, *recJ*, *bapE*, *CCNA_02375*, and *dnaG* (Fig. 2D). DriD-His_6 was also found to bind the *recJ*, *bapE*, *CCNA_02375*, and *dnaG* promoters in vitro with EMSA analyses (Supplemental Fig. S2B).

Transcriptomic analyses demonstrate DriD regulation of several genes

Together, our EMSAs and ChIP studies revealed that DriD bound operator sites within several key promoters, including *recA*, *didA*, and *driD*. To assess whether DriD binding to these promoters impacts transcription, we performed quantitative real-time PCR (qRT-PCR) to measure the transcription of putative target genes in cells following DNA damage. Wild-type (WT) and Δ*driD*::tet^R cells were grown to exponential phase and treated with zeocin to induce double-strand breaks. For WT cells, zeocin treatment led to an ~100-fold induction of *didA* and *bapE* after 45 min and ~10-fold to 20-fold induction of *recA*, *dnaG*, and *recJ* after 90 min. In contrast, for cells lacking *driD*, there was no substantial induction of any of these genes after 45 min and only a significantly reduced level of induction of each gene after 90 min (Fig. 2E). Taken together, our results demonstrate that DNA damage induces

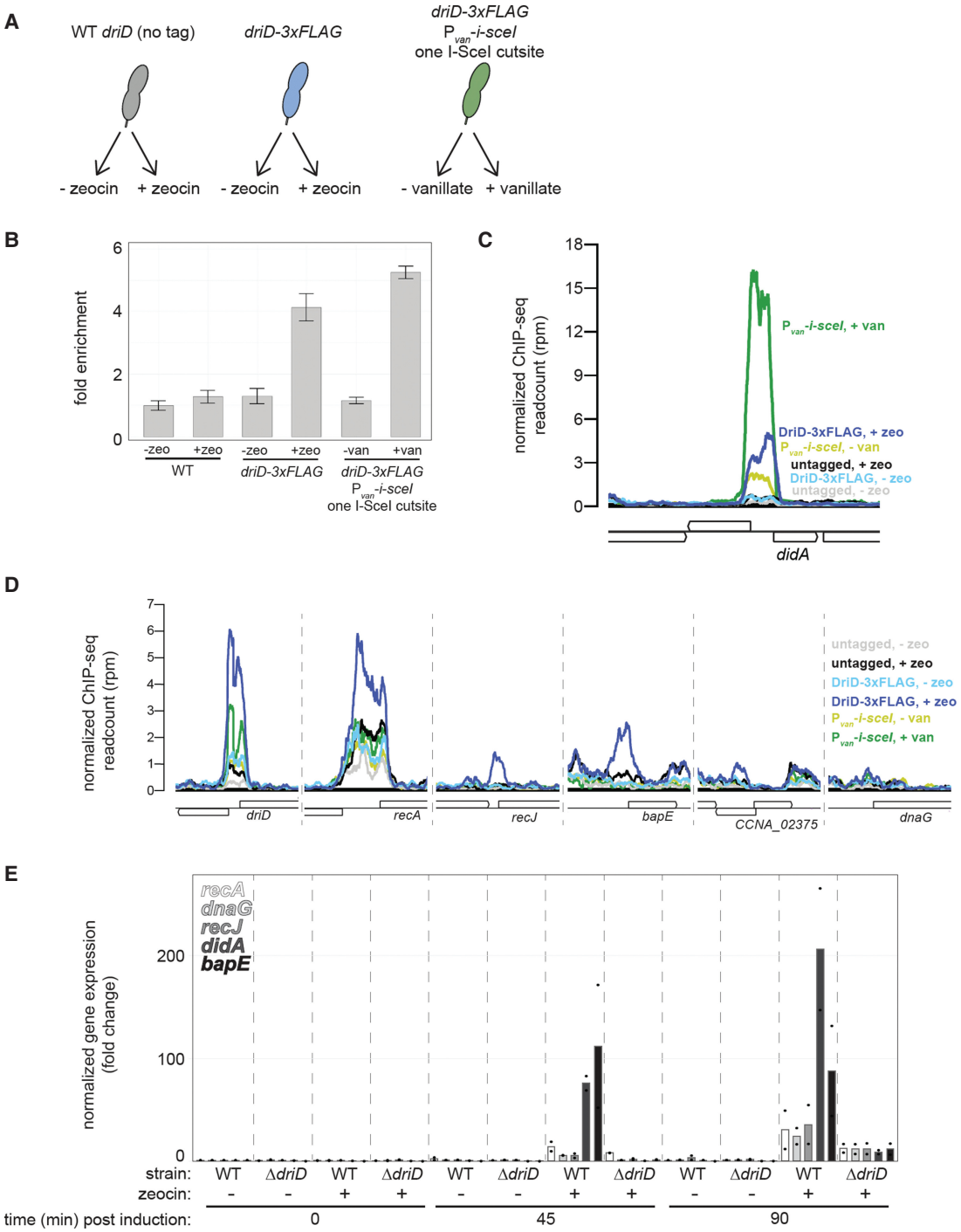

Figure 2. DriD-3xFLAG binds several promoters around the genome during DNA damage in vivo. (*A*) Schematic of strains and treatments for ChIP-seq of DriD during DNA damage. WT cells bearing an untagged *driD* at the native locus and cells with *driD* replaced by a C-terminal-tagged *driD-3xFLAG* at the native locus were grown to mid-exponential phase and treated with or without zeocin. Cells bearing *driD-3xFLAG* at the native locus and an inducible double-strand break system using I-SceI were grown up to mid-exponential phase and treated with or without vanillate to induce a single double-strand break on the genome in each cell. (*B*) Quantitative PCR of the *didA* promoter in ChIP samples compared with input DNA control from the indicated conditions. Fold enrichment = (*didA* signal in ChIP sample/*didA* signal in input)/(control gene signal in ChIP/control gene signal in input). (*C*) ChIP-seq profiles of DriD-3xFLAG at the *didA* promoter. Read counts were normalized globally to the WT untreated condition and are plotted as reads per million (rpm) at each nucleotide position. (*D*) Identified peaks of ChIP-seq profiles of DriD-3xFLAG in the six conditions at various promoters around the genome. Read counts were normalized to the WT untreated condition and are plotted as reads per million (rpm) at each nucleotide position. (*E*) qRT-PCR of five genes at 0, 45, and 90 min after zeocin treatment in WT and Δ*driD* cells. Mean fold change of gene expression relative to the WT untreated 0-min time point are plotted as bars, with biological duplicates indicated as individual points.

DriD to localize to several promoters around the genome and induce gene expression. Given that DriD acts as an activator and previous results suggest the cellular concentration of DriD does not change upon DNA damage (Modell et al. 2014), we next sought to gain insight into possible post-translational regulation of DriD.

Crystal structure of DriD(73–327)

DriD contains a predicted N-terminal helix–turn–helix (HTH) motif and C-terminal region. To gain insight into DriD function and possible signaling via its C-terminal region, we crystallized DriD(73–327). The structure was solved by selenomethionine SAD and refined to final R_{work}/R_{free} values of 23.0%/27.9% to 2.45 Å resolution (Supplemental Tables S1, S2). The structure contains two DriD subunits in the crystallographic asymmetric unit (ASU), which forms a dimer, and density is visible for residues 136–327 of each subunit (Fig. 3A). Residues 73–135, which are disordered in both subunits, form a connecting region to the N-terminal HTH, which is predicted to lie within the first 50 residues of the DriD protein. Our DriD(73–327) structure shows that residues 136–327 adopt a two-domain organization, with residues 136–234 comprising a WYL motif-containing domain and residues 245–327 folding into a separate WCX domain that mediates dimerization. Size exclusion chromatography (SEC) experiments revealed a molecular weight (MW) of 67.1 kDa for DriD, which is consistent with a dimer. Similarly, a MW of 67.5 kDa was obtained in a complex of DriD with a 20mer ssDNA (Supplemental Fig. S3A).

The WYL and WCX domains are connected by a linker consisting of residues 236–244. The DriD WYL domain contains a five-stranded, highly twisted antiparallel β sheet with two α helices packed against one side of the sheet; the topology is (β1: residues 137–139, α1: 148–160, β2: 164–168, β3: 175–187, β4: 191–197, β5: 204–207, and α2: 228–235). β1 is domain-swapped from the other subunit in the dimer and forms part of the WYL domain β sheet (Fig. 3A). The C-terminal dimer domain contains a four-stranded, antiparallel β sheet flanked on one side by two α helices and a long C-terminal helix, with topology (β6: 245–251, α3: 257–261, β7: 269–273, β8: 276–284, α4: 287–297, β9: 301–305, and α5: 307–325). Helix 4 and the C-terminal helix 5 interface with the same helices of the other subunit to create a four-helix bundle dimerization module that buries 2520 $Å^2$ protein buried surface area (BSA), which is on par with BSA observed in physiologically relevant dimers.

Drid(73–327) crystal structure captures bound ssDNA ligand

Markedly, the connection between the WYL and dimer domain in one subunit of the DriD dimer is flexible and, as a result, the density for most of the WYL domain of this subunit is poorly defined. This is reflected in the high B factors of this domain compared with the rest of the structure (Supplemental Fig. S3B). This flexibility is not observed on the other DriD subunit, which has well-defined electron density for the entire WYL domain. Strikingly, in this DriD subunit, extra density was evident after construction of the protein, which could be readily fit with 3 nt of a ssDNA molecule (Fig. 3B). The ssDNA had not been added during crystallization, indicating that it copurified from the *E. coli* expression system.

DriD makes numerous contacts to the bound ssDNA. These interactions are provided by residues from the WYL domain, the dimer domain, and the linker between the domains. Specifically, β strands β2, β4, and β5, as

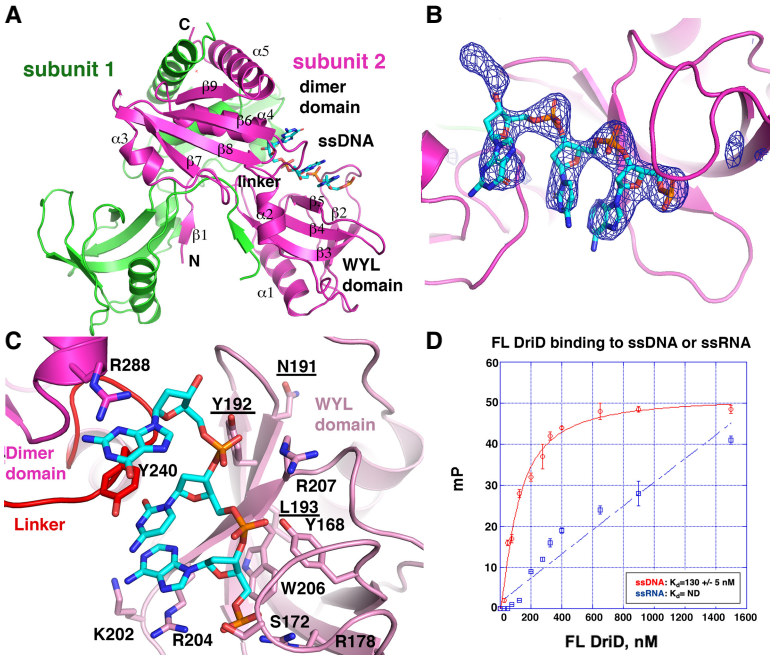

Figure 3. Crystal structure of DriD(73–327). (*A*) Ribbon diagram showing the overall structure of DriD (73–327). DriD(73–327) is a dimer composed of a WYL domain and dimer domain. One subunit is colored magenta and the other is green. ssDNA found bound to the magenta subunit is shown as sticks, and the subunits are labeled. (*B*) Omit σ-A weighted $mF_o - DF_c$ map contoured at 3.7 σ in which the ssDNA was not included in the refinement, revealing clear density for three ssDNA base pairs. (*C*) Closeup of DriD–ssDNA contacts, with interacting residues shown as sticks and labeled. (*D*) Fluorescence polarization (FP) binding isotherm showing interaction of FL DriD with fluoresceinated ssDNA (red) and ssRNA (blue). The binding isotherms are representative curves from three technical repeats, with error bars representing range of values within each measurement. FL DriD binds ssDNA with a K_d of 115 nM ± 14 nM. Binding to ssRNA was not saturable in this DriD concentration range. (ND) Not determined. The error in K_d was determined as the SD between the calculated K_ds for three runs.

well as the long loop between β2 and β3 from the WYL domain, residues 240–242 from the linker region, and residues from α4 of dimer domain all contact the ssDNA molecule (Fig. 3C; Supplemental Movie S1). Formation of this complex orders the residues of the linker between the WYL and dimer domains, which have very poorly defined electron density in the ssDNA-free DriD subunit. The presence of interactions from all three DriD C-terminal regions therefore not only affixes the bound ssDNA to DriD but also helps fold the linker region and anchors the WYL domain to the dimer domain.

In the DriD–ssDNA subunit, the ssDNA bases insert into a pocket created by the linker and β2 and β3 of the WYL domain (Fig. 3C; Supplemental Fig. S4). These regions within the WYL domain serve as the main platform for ssDNA ligand binding. DriD contains a degenerate WYL motif, corresponding to residues 191–193 (NYL) located on β4 (Fig. 3C). The tyrosine from the DriD WYL motif, Tyr192, hydrogen bonds with a ssDNA phosphate moiety. Residues from β3 next to the WYL motif also contribute to ssDNA binding. β3 residue Trp206 packs against one of the nucleotides of the bound ssDNA. Lys202 makes electrostatic interactions with the nucleotides, while Arg204 participates in cation-π interactions with a base (Fig. 3C). Tyr168, Ser172, and Arg178 from strand β2 and the loop connecting strands β2 and β3 contribute hydrogen bonds with the phosphate backbone. Residue Tyr240 from the linker region makes an intercalating interaction between two of the bases in the bound ssDNA. Finally, Arg288 from the dimer domain makes stacking interactions with a DNA base (Fig. 3C). The stacking interactions with ssDNA and the Arg288 and Tyr240 side chains provide stability to the complex but not specificity. Indeed, none of these interactions provide base-specific contacts to any of the nucleotides of the ssDNA molecule. The electron density also did not indicate a specific base at any of the nucleotide positions (Fig. 3B).

Fluorescence polarization (FP) experiments show ssDNA binding to DriD

Our structure revealed ssDNA as a possible signaling ligand for DriD. To test this hypothesis and quantify the interaction between DriD and ssDNA, we next used fluorescence polarization (FP) DNA binding experiments. Measurements were made investigating FL DriD and DriD(73–327) binding to a fluoresceinated 9mer ssDNA fragment, 5′-TAGTCTACT-3′. The proteins bound ssDNA with similar K_ds, from 130 to 250 nM (Fig. 3D; Supplemental Fig. S5). Although the density in our structure was most consistent with ssDNA, we also analyzed binding to the ssRNA substrate, 5′-UAGUCUACU-3′. These experiments showed that ssRNA was able to bind DriD but with lower affinity (Fig. 3D). Modeling an ssRNA into the pocket shows that the presence of the 2′ hydroxyl groups may lead to clashing with some ligand binding residues, such as Tyr240 and Arg288 (Supplemental Fig. S6).

High-resolution DriD–ssDNA structure captures ssDNA bound at both interfaces of the dimer

Our DriD structure captured a ssDNA ligand bound between the WYL and dimerization domains in one of the subunits of the DriD dimer, and our FP analyses support that ssDNA binds DriD with nanomolar affinity. Collectively, these data support ssDNA as a DriD ligand. However, it was not clear whether each subunit in the DriD dimer can bind ssDNA simultaneously, and also unclear is the minimal size of ssDNA molecule required for DriD binding. Hence, we next crystallized DriD in the presence of 9mer ssDNA, 5′-TAGTCTACT-3′. Because residues 75–134 were not visible in our previous structure, we made a construct, DriD(126–327), which excluded most of the disordered residues. Crystals of DriD(126–327) grown in the presence of the 9mer were obtained that diffracted to 1.65 Å resolution, and the structure was solved and refined to final R_{work}/R_{free} values of 19.1%/22.3% (Materials and Methods). This structure revealed the same DriD dimer as observed in our previous DriD(73–327) structure (Fig. 4A). In addition, clear density was observed for ssDNA bound in the same location as the previous structure, between the WYL and dimer domains. However, in this structure, both DriD subunits contain bound ssDNA (Fig. 4B; Supplemental Movie S2). The DriD–ssDNA contacts observed in one subunit are identical to those found in our previous structure (Fig. 4C), while the DriD–ssDNA interactions observed in the other subunit show only a few differences that appear to be due to crystal packing. In particular, in the latter subunit, base stacking interactions from the linker residue Tyr240 are not present. Interestingly, however, linker residue His241 functionally replaces the tyrosine, making similar interactions with the ssDNA (Fig. 4D).

While a 9mer DNA site was used for crystallization of this complex, the structure shows that 3 bp of the ssDNA account for most of the contacts to DriD, with the fourth nucleotide located 5′ to the 3 bp, contributing additional interactions (Fig. 4C,D). In one subunit, the fourth nucleotide is partially shielded by the long loop between β4 and β5, and Glu197 interacts with the fourth base (Fig. 4D). This indicates that short regions of ssDNA (3–4 bp) are all that is required for effective DriD binding. Crystal packing interactions to the ends of the ssDNA that affix it in a particular position, along with the high resolution of the data, allowed us to specifically assign the nucleotides bound at each DriD subunit. However, as observed in the DriD(73–327)–ssDNA structure, there were no contacts from either DriD subunit that mediated base specificity. As observed in our previous structure, ssDNA binding to each of the two subunits resulted in stable anchoring of the domains, with both WYL domains exhibiting well-defined electron density.

In vitro and in vivo tests of structure-based model

Our data indicate ssDNA is a ligand for DriD. However, to assess whether ssDNA binding affects operator DNA binding and transcription activation by DriD, we next

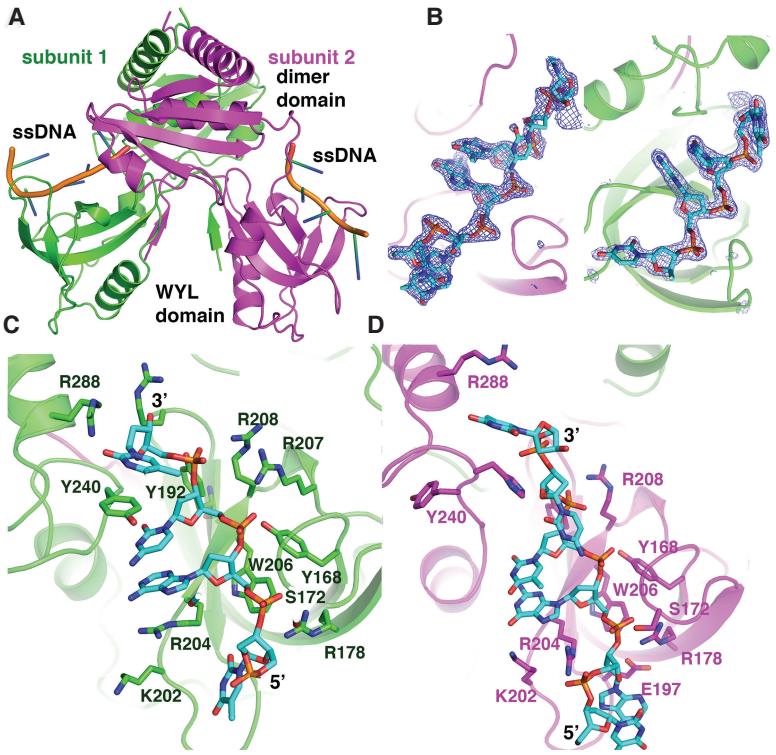

Figure 4. Crystal structure of DriD bound to 9mer ssDNA. (*A*) Ribbon diagram showing the overall DriD–ssDNA structure. The subunits of the dimer are colored magenta and green, and each contains a bound ssDNA. (*B*) Omit $mF_o - DF_c$ map contoured at 3.4 σ in which the ssDNA was not included in the refinement. (*C*,*D*) Closeup of DriD–ssDNA contacts, with interacting residues shown as sticks and labeled for each subunit.

performed in vitro and in vivo experiments. We first analyzed DNA operator binding by FL DriD and DriD(73–327) to establish whether the predicted N-terminal HTH domain of DriD is responsible for operator binding. No binding was observed to the fluoresceinated operator by DriD(73–375) in the presence or absence of ssDNA. In contrast, FL DriD bound the operator DNA site robustly and with high affinity, which was enhanced by the addition of ssDNA (Fig. 5A); FL DriD bound the operator with a K_d of 25 nM ± 6 nM in the absence of ssDNA and 5 nM ± 1 nM in the presence of ssDNA. The slightly higher affinity observed for DriD binding to operator DNA in FP studies compared with EMSA may be because the DNA used for FP contains only the operator site (DriD displays some nonspecific binding), and also the FP DNA contains an optimized operator site. Also, slightly different buffer conditions were used. One caveat with our FP experiments is that we were not able to completely remove all ssDNA from the DriD preparations, indicating that the effect of ssDNA may be even more significant than observed. Thus, to better test the importance of ssDNA binding, we next generated mutations in DriD ssDNA binding residues and used FP to measure the effect of these substitutions on operator binding.

DriD mutants DriD(Y168A), DriD(R176A–R178A), and DriD(Y168A–R178A–Y192A–R204A) were generated, and purified proteins were produced. FP analyses showed that DriD(R176A–R178A) and DriD(Y168A–R178A–Y192A–R204A) showed essentially no binding to ssDNA, while the DriD(Y168A) mutant displayed an ~10-fold reduction in ssDNA binding compared with WT (Supplemental Fig. S7). Next, FP binding to operator DNA was measured via FP by the FL WT DriD and the mutant proteins in the presence of ssDNA. In these experiments, the DriD(Y168A) protein bound the DNA operator with a K_d of 22.3 nM ± 7 nM (compared with 5 nM ± 2 nM for WT), while the DriD(R176A–R178A) mutant showed weak, nonsaturable binding. Finally, the multimutant DriD, DriD(Y168A–R178A–Y192A–R204A), displayed no binding to the operator site (Fig. 5B). Again, because none of the mutations were located in the HTH, which we established is responsible for operator DNA binding, these data indicate that ssDNA binding to the C-terminal region of DriD functions acts as an allosteric regulator to stimulate DriD operator DNA binding.

To probe the effects of mutating residues in the ssDNA binding site of DriD on its ability to function as a transcription activator, we developed a transcriptional reporter system (Modell et al. 2014). The reporter strain bears a transcriptional fusion of the *didA* promoter to *lacZ* integrated at a distal locus on the genome, a clean deletion of *didA*, and a marked deletion of *driD*. Into this strain, we transformed a vector containing no *driD*, a WT copy of *driD*, or various point mutations of *driD* where changes to key residues involved in ssDNA binding were made. We then treated each of these strains with zeocin to induce DriD-mediated activation of the *didA* reporter. As expected, we saw activation in the original WT strain with the endogenous *driD* still intact, and this was completely abolished in the *driD* deletion strain or the deletion strain carrying an empty vector. *didA* expression was induced in cells bearing the plasmid-borne WT copy of *driD*, as expected, albeit somewhat lower than the native state. This difference may derive from altered

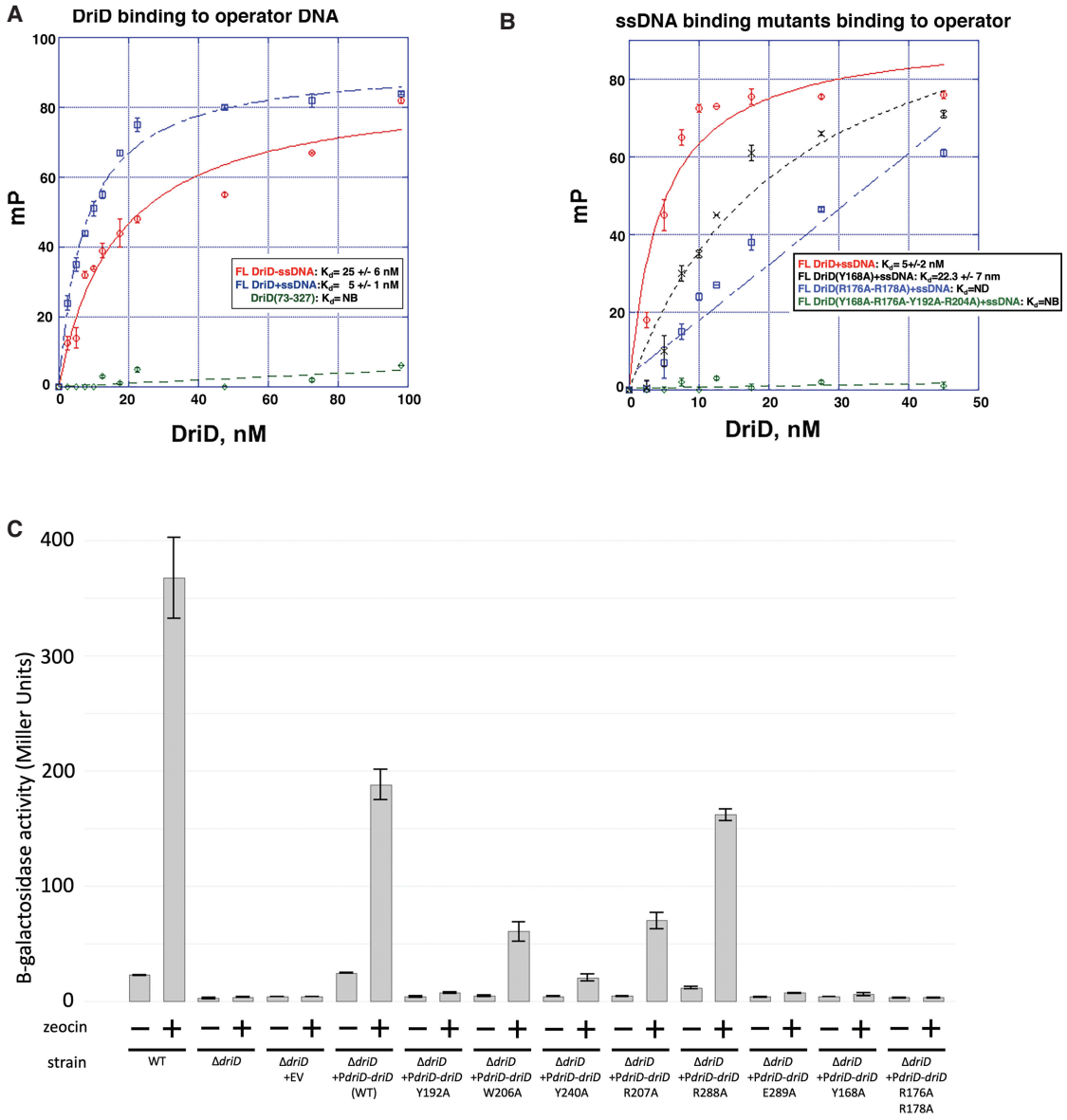

Figure 5. ssDNA stimulates the operator DNA binding activity of DriD. (*A*) FP binding isotherm showing binding of DriD(73–327) to operator DNA in the presence of ssDNA (green), FL DriD binding to operator DNA in the absence of ssDNA (red), and FL DriD binding to operator DNA in the presence of ssDNA (blue). FL DriD bound the operator with a K_d of 25 nM ± 6 nM in the absence of ssDNA and 5 nM ± 1 nM in the presence of ssDNA. No binding was observed for DriD(73–327) (indicated by "NB"). (*B*) FP binding isotherms of DriD proteins with substitutions in the ssDNA binding site to assess the role of ssDNA binding as an allosteric regulator of DriD operator binding. In these studies, the DriD(Y168A) protein bound the DNA operator with a K_d of 22.3 nM ± 7 nM (compared with 5 nM ± 2 nM for WT), while the DriD(R176A–R178A) and DriD(Y168A–R178A–Y192A–R204A) mutants showed nonsaturable and no binding, respectively. (ND) Not detectable or not measurable, (NB) no binding. The *Y*-axis and *X*-axis are millipolarization (mP) units and DriD concentration (in nanomolar [nM]), respectively. Representative binding curves are shown. The experiments were performed in technical triplicates, and the reported error in K_d was determined as the SD between the calculated K_ds for three runs. (*C*) β-Galactosidase assay measuring transcriptional activity of a P_{didA}-*lacZ* reporter in either WT or cells lacking the native copy of *driD* and complemented with various *driD* mutation constructs ($n = 3$; error bars indicate SD). Exponential phase cells were assayed after 45 min of treatment with or without zeocin.

expression levels between the native, chromosomal conformation versus the multicopy plasmid-borne version, as well as potential feedback regulation of DriD binding to its own promoter. Single substitutions in key ssDNA binding residues, such as Y192A, Y240A, and R207A, significantly impaired the ability of DriD to activate transcription. The Y168A and R176A–R178A mutations completely abrogated transcriptional activation by DriD, mirroring complete inactivation seen with the *driD* deletion and empty vector strains. These data support the conclusion that ssDNA binding is required for DriD to function as a transcriptional activator.

Discussion

The paradigm for bacterial DNA damage and its coordination with the cell cycle is the SOS response (Little and Mount 1982; Jaffé et al. 1986; Erill et al. 2007). This canonical repair system has been found in most bacteria and relies on the formation of ssDNA during DNA damage that bind RecA, driving it to form filaments. The RecA-ssDNA filaments stimulate autocleavage of LexA, the repressor of DNA damage and cell cycle genes (Little et al. 1980; Phizicky and Roberts 1981; Galletto et al. 2006). Recent work uncovered the first damage-induced, SOS-independent response in *C. crescentus* and showed that the transcription regulator, DriD, activates this pathway (Modell et al. 2014). However, the molecular mechanisms by which DriD senses DNA damage and activates the transcription of DNA damage genes have been unclear. Here we show that DriD acts as a transcription activator of several key genes involved in DNA damage response and cell cycle control, including *recA*, *driD*, and the cell division inhibitor *didA*. Our data demonstrate that DriD binds with high affinity and specificity to a 20-bp palindromic DNA site using residues within its predicted N-terminal, HTH domain.

Our crystal structure of DriD(73–327) captured ssDNA bound at the interface between the DriD WYL and dimer domains that comprise the C-terminal region of DriD. This finding is striking in light of data showing that the generation of double-strand breaks stimulates DriD activity, as double-stranded breaks are repaired by a mechanism involving the partial resection of DNA, which produces ssDNA for homologous recombination (Symington 2014; Bell and Kowalczykowski 2016). In *C. crescentus* the AddAB complex, composed of the AddA helicase and AddB nuclease, is known to process double-stranded breaks to produce ssDNA (Martins-Pinheiro et al. 2007; Badrinarayanan et al. 2015). Thus, these data are consistent with DriD sensing DNA damage through the formation of ssDNA. Structures of ssDNA-bound and free subunits of DriD revealed that ssDNA binding leads to an ordering of the WYL domain relative to the dimer domain, which would be transmitted to the N-terminal DNA binding domain. To test this structure-based hypothesis, we performed biochemical and in vivo assays. These experiments demonstrated that substitution of key DriD ssDNA binding residues significantly impaired or abrogated the ability of DriD to bind its operator DNA site and activate transcription. Thus, these combined data indicate that ssDNA acts as an allosteric signal by binding DriD and affecting its ability to act as a transcription activator. Further studies dissecting the role and origin of the ssDNA bound by DriD in vivo; the role of double-strand break repair machinery, such as the helicase–nuclease complex AddAB, which resects DSB ends to reveal sections of ssDNA; and the interplay and potential competition with other ssDNA binding proteins (namely, the cell's main recombinase, RecA) will provide insight into DriD's role in the cell under differing cellular stresses.

Numerous proteins that contain WYL domains have been identified. Transcription regulators that harbor WYL motifs include PafBC and BrxR proteins, while WYL domain-containing proteins that function in regulating catalysis include the PIF1 helicase, which contains an activating WYL domain, and the accessory WYL1 protein, which enhances Cas13d activity (Andis et al. 2018; Yan et al. 2018; Müller et al. 2019; Zhang et al. 2019; Luyten et al. 2022). The WYL-containing BrxR family of transcriptional factors was recently revealed as regulators of phage defense systems, such as bacteriophage exclusion (BREX) phage restriction systems. Bioinformatic analyses suggest that these regulators and associated phage defense systems appear to be widespread among bacteria (Picton et al. 2021, 2022; Luyten et al. 2022). Recently reported structures of BrxR proteins have shown they contain a WYL domain and C-terminal dimer domain (Luyten et al. 2022; Picton et al. 2022); thus, they harbor an overall architecture similar to that of DriD. However, the structure of the BrxR dimer domain and its mode of dimerization are distinct from DriD. In addition, while BrxR proteins bind with high affinity to palindromic DNA operator sites, similar to DriD, BrxR family members function as transcriptional repressors rather than activators. Why phage defense genes such as BREX are normally repressed is unclear, but data indicate that the phage defense genes may be toxic to the cell (Luyten et al. 2022; Picton et al. 2022). Hence, their repression by WYL proteins is needed to reduce fitness costs to the host prior to phage infection. Small molecule/effector binding to these proteins is therefore required to induce them from the DNA. The ligands for BrxR and related regulators have thus far not been discovered, but nucleotides or nucleic acids have been suggested as possibilities for inducing ligands for these proteins (Luyten et al. 2022; Picton et al. 2022).

The WYL protein showing the most similarity to DriD is the mycobacterial PafBC complex. Like DriD, the PafBC complex is a DNA damage response regulator (Supplemental Fig. S8). In mycobacteria, PafBC is responsible for activating transcription of ~150 genes induced by DNA damage (Olivencia et al. 2017; Müller et al. 2018). The crystal structure of the FL *A. aurescens* PafBC was solved in its apo form and revealed that it harbored a domain organization similar to that of DriD, with an N-terminal HTH domain connected to a WYL domain and a dimer domain. Notably, the *A. aurescens* PafBC protein exists as a tandem fusion; the single protein encodes two sequential HTH–WYL–WCX fragments that are covalently linked. Most PafBC complexes, however, are formed from two homologs, PafB and PafC (proteasome accessory factors B and C) (Müller et al. 2019), encoded together in an operon that is closely associated with the bacterial proteasome gene locus. The close genetic association between the Paf proteins and the proteasome is consistent with the fact that, in mycobacteria, many repair proteins are removed by proteasomal degradation following the completion of DNA damage repair. Notably, recombinant, purified PafBC complex is unable to bind its identified DNA operator site. This suggests the details of the activation mechanisms between PafBC and DriD differ, as DriD binds its palindromic DNA site with high affinity in vitro. Furthermore, DriD binds to promoters containing

−35 and −10 promoter elements, while PafBC-activated promoters lack functional −35 motifs.

Interestingly, in the *A. aurescens* PafBC structure, one of the HTH domains is wedged into the protein core composed of the WYL and dimer domain, such that residues within its recognition helix were completely inaccessible. Overlay of the dimer domain of our DriD–ssDNA structure onto the PafBC dimer domain shows that ssDNA binding results in a shifting of the DriD WYL domain relative to its position in apo PafBC, which would result in the ejection of the HTH to avoid clashing. This conformational change would thus expose the HTH, allowing it to bind DNA (Supplemental Fig. S8). Moreover, the interaction of the ssDNA with its WYL domain would prevent its association with an HTH. Hence, ssDNA binding may function not only to order the DriD domains, but also to induce a reorganization of the structure to free the HTH binding domains and allow their interaction with DNA. Support of this mechanism for PafBC comes from a recent report by Müller et al. (2021) using biochemistry and cryo-EM to interrogate PafBC binding to RNAP and a promoter containing a PafBC binding site. Biochemical analyses showed that ssDNA could activate the ability of PafBC to interact with RNAP on promoters that contain PafBC operator sites. However, while cryo-EM structures were obtained, the reconstructions did not reveal the ssDNA, and the density for both the WYL and WCX domains was weak; hence, the domains were not included in the deposited coordinates (Müller et al. 2021). However, these data provide support that ssDNA functions as a ligand for WYL-containing transcriptional regulators.

Sequence alignments of multiple DriD homologs from α-proteobacteria show that residues in the DriD structure shown to be key in ssDNA binding are highly conserved (Supplemental Fig. S9). Specifically, Tyr168, Arg176, Arg178, Tyr192, Arg204, and Arg207 are conserved in homologs. Our structures show that DriD residues Ser172 and Lys202 make weak phosphate interactions to the nucleotides and thus are not as critical to ssDNA binding; consistent with this, these residues are not as conserved. Nonetheless, Ser172 is typically either a serine or threonine, and Lys202 is either a lysine or arginine in most DriD homologs. Tyr240 is located in the linker domain between the WYL and dimer domains and makes key stacking interactions. In DriD homologs, this residue is either a tyrosine or phenylalanine. Although mostly conserved as an arginine, residue 288 is also found to be a leucine in homologs. However, this residue mediates stacking interactions with a base in the ssDNA, which modeling shows a leucine side chain could accomplish. Strikingly, while the *A. aurescens* PafBC structure is not in the activated conformation, superpositions of the WYL domains of the *A. aurescens* PafB and PafC regions onto the WYL domain of DriD revealed that, although the sequence identity between DriD and PafBC is only 11%, the key ssDNA binding residues observed in DriD are conserved in PafB and PafC (Fig. 6A,B). Thus, our DriD–ssDNA structures provide the first molecular view of ssDNA ligand binding by a WYL motif-containing protein, and our data support that this could potentially represent a conserved mode of allosteric regulation among some WYL proteins. Finally, non-SOS DNA damage response systems are poorly understood. Our data reveal the first molecular details of ligand-mediated activation of such a system.

Materials and methods

Growth conditions

All *Caulobacter* strains were grown in rich medium (PYE) at 30°C. Antibiotics were used at the following concentrations for strain construction and plasmid maintenance in *Caulobacter* strains in liquid:plates: 5 μg/mL:25 μg/mL kanamycin and 1 μg/mL:2 μg/mL oxytetracycline. Transformations and transductions were performed as previously described (Ely 1991).

Plasmid and strain construction

Plasmids and *Caulobacter* strains used in this study are listed in Supplemental Tables S3 and S4, respectively. DNA oligonucleotides used in strain construction and experiments are listed in Supplemental Table S5. *Caulobacter crescentus* CB15N genomic DNA was used as a template for PCR amplifications unless noted otherwise. PCR was performed with Phusion HF DNA polymerase with 5× Phusion GC reaction buffer (NEB). Each reaction contained 10 μL of buffer, 4 μL of dNTPs, 5 μL of a 10 μM forward and reverse primer mix, 50 ng of template, 10 μL of 3 M betaine monohydrate (Sigma), 1 μL of DMSO, 0.5 μL of polymerase, and nuclease-free water to 50 μL. Two-step cycling was performed as follows: 30 sec at 98°C, 34 times for 10 sec at 98°C and 30 sec/kb at 72°C, and 5 min at 72°C. Fusion PCR was performed similarly with 50 ng of the largest template fragment and equimolar amounts of the shorter template fragments, with an additional annealing step of 20 sec at 60°C. All PCR products were either digested with the noted restriction enzymes and ligated into the double-enzyme cut corresponding plasmid or were Gibson assembly-cloned into double-enzyme cut corresponding plasmid following the manufacturer's instruction. Five microliters of ligation reactions was subsequently transformed into chemically competent *E. coli* DH5α cells. All resulting plasmids were verified by Sanger sequencing. For strain construction, gene insertions and deletions were verified by PCR using primers outside the genetic alteration, as appropriate.

To generate pNPTS138::Δ*driD*::tet^R, a 600-bp region upstream of *driD* that included the first 9 nt of *driD* was amplified by PCR using primers oKRG259 and oKRG260. A 600-bp region downstream from *driD* including the last 9 nt of *driD* was amplified by PCR using primers oKRG261 and oKRG262. The tetracycline resistance cassette was amplified by PCR using primers oKRG440 and oKRG441 with the previously described pMCS-5 (Thanbichler et al. 2007) as a template. These three PCR products were fused using fusion PCR with primers oKRG259 and oKRG262, gel-purified, digested, and ligated into an EcoRI-cut pNPTS138.

To generate pRVMCS-2::P_{driD}-*driD*, a region spanning ~400 bp of the promoter of *driD* and the *driD*-coding region was amplified by PCR using primers oKRG316 and oKRG317. The PCR product was digested with SacI and SacII and cloned into SacI/SacII-cut pRVMCS-2(kan^R).

To generate the plasmids pRVMCS-2::P_{driD}-*driD*(Y192A), pRVMCS-2::P_{driD}-*driD*(W206A), pRVMCS-2::P_{driD}-*driD*(Y240A), pRVMCS-2::P_{driD}-*driD*(R207A), pRVMCS-2::P_{driD}-*driD*(R288A), pRVMCS-2::P_{driD}-*driD*(E289A), and pRVMCS-2::P_{driD}-*driD*

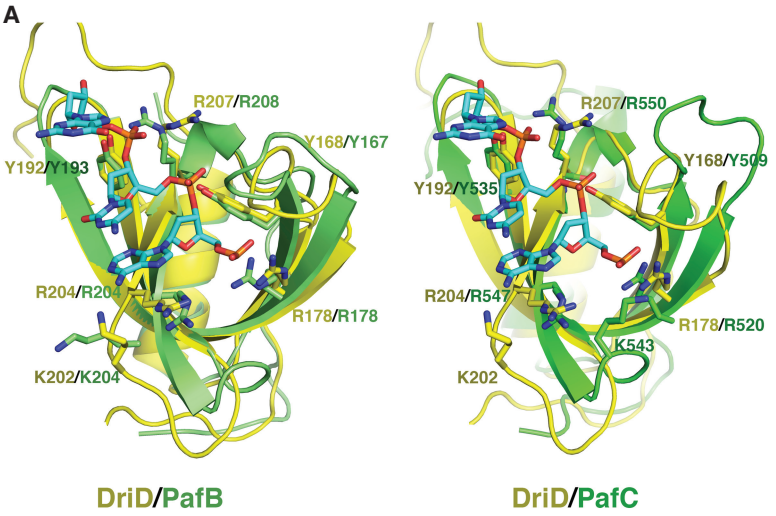

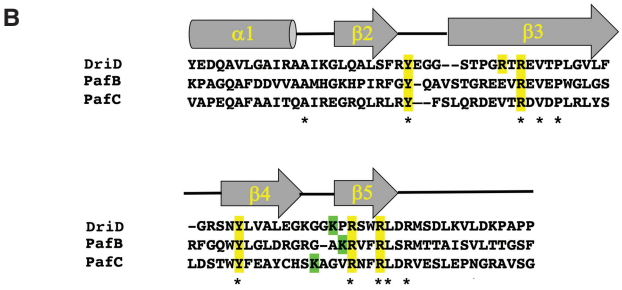

Figure 6. Key ssDNA binding residues in DriD are conserved in PafB and PafC. (*A*, *left*) Overlay of the WYL domains of DriD (yellow) and PafB (lime) from the *A. aurescens* PafBC structure (6SJ9). Residues involved in ssDNA binding by DriD are shown as sticks, as are the corresponding residues in those locations in PafB. (*Right*) Overlay of the WYL domains of DriD (yellow) and the PafC domain (green; 6SJ9). Residues involved in ssDNA binding in DriD and the corresponding residues in the PafC domain are shown. Notably, the key DriD ssDNA binding residues are conserved in both PafB and PafC. (*B*) Structure-based sequence alignment of the WYL domains of DriD, PafB, and PafC. Residues that contact ssDNA in DriD and are conserved in PafB and PafC are highlighted in yellow. ssDNA binding residues that are not completely conserved are colored green. Secondary structural elements from the DriD structure are indicated *above* the alignment. Identical residues in all three sequences are indicated by asterisks *below* the alignment.

(Y168A), each mutation was introduced into pRVMCS-2(*kan*^{R}) using round-the-horn mutagenesis with the following pairs of primers: oKRG362/oKRG365, oKRG366/oKRG369, oKRG370/oKRG373, oKRG374/oKRG377, oKRG378/oKRG381, oKRG382/oKRG385, oKRG386/oKRG389, and oKRG390/oKRG393, respectively.

To generate pRVMCS-2::P$_{driD}$-*driD*(R176A-R178A), a region spanning from the promoter to codon 175 of *driD* was amplified by PCR using primers oKRG317 and oKRG529. The region spanning from codon 176 to 15 bp after the stop codon of *driD* was amplified by PCR using primers oKRG530 and oKRG316. The two PCR products were fused using fusion PCR with primers oKRG316 and oKRG317, gel-purified, digested, and ligated into a SacI/SacII-cut pRVMCS-2(*kan*^{R}).

To generate pRVMCS-2::P$_{driD}$-*driD-his*$_6$, a region spanning ~400 bp of the promoter of *driD* and the *driD*-coding region was amplified by PCR using primers oKRG561 and oKRG562. The PCR product was digested with SacI and SacII and cloned into AflII/SacII-cut pRVMCS-2(*kan*^{R}).

To generate strains ML3756 and ML3757, the inserts in plasmids pNPT138-*driD*::*driD-3xFLAG* and pNPTS138-Δ*driD*::*tet*^{R} were introduced by two-step recombination into CB15N, respectively.

To generate strain ML3758, the insert in plasmid pNPTS138-*driD*::*driD-3xFLAG* was introduced by two-step recombination into ML2169. Next, the I-SceI site marked with a *tet*^{R} cassette at *ccna_00727* and the P$_{van}$-*i-sceI*-inducible restriction enzyme marked by a *chl*^{R} cassette were sequentially introduced with transduction mediated by the transducing phage Cr30.

To generate strains ML3759, ML3760, ML3761, ML3762, ML3763, ML3764, ML3765, ML3766, ML3767, ML3768, and ML3835, the plasmids pRVMCS-2(*kan*^{R}), pRVMCS-2::P$_{driD}$-*driD*(Y192A), pRVMCS-2::P$_{driD}$-*driD*(W206A), pRVMCS-2::P$_{driD}$-*driD*(Y240A), pRVMCS-2::P$_{driD}$-*driD*(R207A), pRVMCS-2::P$_{driD}$-*driD*(R288A), pRVMCS-2::P$_{driD}$-*driD*(E289A), pRVMCS-2::P$_{driD}$-*driD*(Y168A), pRVMCS-2::P$_{driD}$-*driD*(R176A R178A), and pRVMCS-2::P$_{driD}$-*driD-his*$_6$ were introduced by electroporation to ML3757, respectively.

Bioinformatic analyses of promoters

Promoter regions upstream of genes found to be bound by DriD, shown in Supplemental Figure S2, were extracted from the WT *Caulobacter crescentus* genome NC_011916.1. +1 transcription start site prediction was informed by previous global identification of transcription start sites (Zhou et al. 2015). For genes with unannotated start sites, unpublished RNA-seq reads of *C. crescentus* were used to inform putative +1 sites; −10 and −35 sites were identified based on proximity to predicted +1 sites.

Expression and purification of C. crescentus *full-length DriD, DriD(73–327), DriD(126–327), DriD(Y168A), DriD(R176A–R178A), and DriD(Y168A–R178A–Y192A–R204A)*

For structural and biochemical studies, the gene encoding *C. crescentus* DriD, which was codon-optimized for expression in *E. coli*, was purchased from Genscript Corporation (http://www.genscript.com) and subcloned into pET15b such that a cleavable His tag was expressed on the protein for purification. Constructs expressing the C-terminal region (residues 73–327 and 126–327) were generated from this gene and subcloned into pET15b to also encode an N-terminal His tag. *E. coli* C41(DE3) cells were

transformed with the expression vectors. DriD mutants DriD (Y168A), DriD(R176A–R178A), and DriD(Y168A–R178A–Y192A–R204A) were generated with QuikChange (Thermo Fisher). Cells with the expression constructs were both grown at 37°C in LB medium with 0.17 mg/mL ampicillin to an OD_{600} of 0.6 and then induced with 0.50 mM isopropyl β-d-thiogalactopyranoside (IPTG) overnight at 15°C. Cells were harvested by centrifugation and then resuspended in buffer A (50 mM Tris-Cl at pH 7.5, 300 mM NaCl, 5% [v/v] glycerol, 0.5 mM β-mercaptoethanol [βME]), with 1× protease inhibitor cocktail. The resuspended cells were then disrupted with a microfluidizer, and cell debris was removed by centrifugation at 15,000 rpm for 45 min at 4°C. The supernatant was loaded onto a cobalt NTA column. The column was washed with 300 mL of 5 mM imidazole in buffer A and eluted in steps with 10, 20, 30, 50, 100, 200, and 500 mM imidazole in buffer A. Fractions were analyzed by SDS-PAGE, and those containing the protein were combined. Proteins used in FP studies were further purified in attempts to remove bound ssDNA by size exclusion using an S200 column. His tags were removed by thrombin digestion overnight at 37°C using a thrombin cleavage capture kit. The cleaved His tags were removed by loading cleavage reactions onto a Ni-NTA column and collecting the flow-through. Tag-free proteins were concentrated using centricons with a 10-kDa MW cutoff. The methionine inhibitory pathway was used to produce selenomethionine (semet)-labeled DriD (73–327) for single-wavelength anomalous diffraction (SAD) experiments. (Doublié 1997). The Semet protein was purified as per the WT. For the purification of DriD-His_6, the encoding region of *driD* was cloned into the pET28b$^+$ vector and transformed into BL21(DE3) *E. coli* cells. The resulting cells were grown at 37°C in LB medium with 30 μg/mL kanamycin to an OD_{600} of 0.6 and then induced with 0.50 mM IPTG for 6 h at 30°C. Cells were harvested by centrifugation and then resuspended in lysis buffer (150 mM NaCl, 50 mM Tris at pH 8, 2 mM $MgCl_2$, 1 mM tris 2-carboxyethyl phosphine hydrochloride [TCEP], 10 μg/mL lysozyme, 0.2 mM phenylmethylsulfonyl fluoride [PMSF]). The resuspended cells were then disrupted with sonication, and cell debris was removed by centrifugation at 15,000 rpm for 40 min at 4°C. The supernatant was passed over a Ni-NTA agarose column pre-equilibrated with lysis buffer, washed with wash 1 buffer (50 mM Tris at pH 8, 500 mM NaCl, 2 mM $MgCl_2$, 1 mM TCEP, 10 mM imidazole) and wash 2 buffer (50 mM Tris at pH 8, 150 mM NaCl, 2 mM $MgCl_2$, 1 mM TCEP, 25 mM imidazole), and eluted with elution buffer (50 mM Tris at pH 8, 150 mM NaCl, 2 mM $MgCl_2$, 1 mM TCEP, 300 mM imidazole). Fractions were analyzed by SDS-PAGE, and those containing the protein were combined.

Electrophoretic mobility shift assays (EMSAs)

Ten-microliter reactions with the indicated concentration of DriD-His_6 and linear dsDNA (20 ng) in binding buffer (10 mM Tris at pH 7.5, 1 mM EDTA, 100 mM KCl, 100 μM DTT, 5% [v/v] glycerol, 100 μg/mL BSA) were incubated for 1 h at 30°C and then placed on ice. Samples were then electrophoresed in a TBE gel for 100 min at 4°C at 100 V, and gels were subsequently stained in SYBR Gold. For substrates ≤40 bp, oligonucleotides were denatured for 2 min at 95°C and allowed to cool slowly to room temperature to promote annealing. DNA substrates >40 bp were generated by PCR as indicated in Supplemental Table S5 and purified using PCR purification kits. Quantification of images was performed with Fiji/ImageJ. The amount of free and bound DNA fragments was determined as fractions of the total intensity across the lane. Prism 8 software was used to fit curves (specific binding with hill slope algorithm) and to determine binding affinities and hill coefficients.

Chromatin immunoprecipitation quantitative PCR (ChIP-qPCR) and sequencing (ChIP-seq)

To generate samples for chromatin immunoprecipitation of FLAG-tagged DriD, WT (untagged *driD*) and *driD*::*driD-3xFLAG* were grown to mid-exponential phase and treated with or without 15 μg/mL zeocin as indicated for 45 min. Additionally, cells bearing both *driD::driD-3xFLAG* and the P_{van}-*i-sceI* single double-strand break system were grown to exponential phase and treated with or without 0.5 mM vanillate as indicated for 45 min. Chromatin immunoprecipitation of DriD-bound complexes was isolated as previously described using α-FLAG M2 agarose beads (Merck) (Guo et al. 2018). Input DNA to be used as a preimmunoprecipitation control for ChIP-PCR was removed prior to addition of the FLAG antibody. Final DNA samples after precipitation were then used directly for ChIP-qPCR analysis or for generating sequencing libraries as previously described (Guo et al. 2018). Paired-end sequencing was performed on an Illumina Hi-Seq 500 at the Massachusetts Institute of Technology Bio Micro Center. ChIP-seq data are available at GEO accession number GSE197978. MACS was used to identify peaks in ChIP samples compared with control conditions with the following command: callpeak -t LaubLab_ChIPseq_antiFLAG_driD-3xFLAG_pluszeo_sorted.bam -c LaubLab_ChIPseq_antiFLAG_WT_pluszeo_sorted.bam -n peaks -g 4042999 –nomodel. Identified peaks were then manually compared with annotated gene locations to identify promoters with DriD-3xFLAG ChIP peaks during zeocin treatment.

Quantitative real-time PCR (qRT-PCR) analysis of gene expression

WT and Δ*driD*::tet^R cells were grown up to exponential phase in PYE at 30°C. RNA was extracted and converted to cDNA for use in qRT-PCR as described previously (Guzzo et al. 2020). Expression of RpoA was used as an endogenous control for each sample. All samples were assayed in technical triplicate and biological duplicate, with standard curves to compare each plate. qRT-PCR was performed on a LightCycler 480 system (Roche) in 384-well plates with the following thermocycler program: 10 min at 95°C, 15 sec at 95°C, 30 sec at 60°C, and 30 sec at 72°C, with 40 cycles of steps 2–4. The LightCycler 480 software was used to calculate the crossing point (Cp) values at the second derivative maximum. Replicate value averages were normalized to the *rpoA* measured value.

Crystallization and structure determination of C. crescentus *DriD(73–327) and DriD(126–327)*

For crystallization, the tag-free DriD proteins were concentrated to ~30 mg/mL. Wizard screens I to IV and cryo screens I and II were used for screening at room temperature by the hanging drop vapor diffusion method. Crystals were produced of DriD (73–327) by mixing the protein 1:1 with a solution consisting of 0.1 M N-(2-hydroxyethyl)piperazine-N′-(2-ethanesulfonic acid) (HEPES; pH 7.5) and 1.5 M ammonium sulphate. The crystals grew at room temperature and obtained their maximum size in 2–3 wk. Crystals were cryopreserved by dipping them in a solution consisting of the crystallization reagent supplemented with 20% (v/v) glycerol before plunging them into liquid nitrogen. X-ray intensity data were collected at Advanced Light Source (ALS) beamline 5.0.2 and processed with XDS (Supplemental Table S1; Kabsch 2010). Crystals of the Semet DriD(73–375) protein were produced as for the native protein, and SAD data were collected at ALS beamline 5.0.2 and processed with XDS (Kabsch et al. 2010). Phenix Autosol (Liebschner et al. 2019) was used to determine selenium sites, perform phasing, and carry out density modification. The resultant experimental SAD map was of

excellent quality, allowing construction of the model by Coot (Emsley and Cowtan 2004). There are two DriD(72–327) subunits in the crystallographic asymmetric unit (ASU). The experimental map revealed density that could not be fit by protein. The initial model was subjected to refinement in Phenix, which improved the phases, allowing the extra density to be readily identified and fit as ssDNA consisting of 3 nt, which were bound to one subunit of the dimer (Supplemental Movie S1). After multiple rounds of rebuilding in Coot and refinement in Phenix (Liebschner et al. 2019), the structure converged to R_{work}/R_{free} values of 23.0%/27.9% to 2.45 Å resolution (Supplemental Table S2). Density was evident for residues 136–327 of each subunit, with the N-terminal residues being disordered. As a result, a shorter construct, DriD(126–327), was generated and used in subsequent crystallization experiments.

Crystals were obtained of a 1:1.5 complex of DriD(126–327) with the 9mer ssDNA, 5′-TAGTCTACT-3′, mixed 1:1 with a crystallization solution consisting of 0.1 M 2-(N-morpholino) ethanesulfonic acid (Mes; pH 6.5), 0.1 M imidazole, and 20% (w/v) PEG 8000. The crystals were produced at room temperature and grew to their maximum size in 1 wk. The crystals were cryoprotected by dipping them for 2–4 sec in the crystallization solution supplemented with 25% (v/v) glycerol before plunging them into liquid nitrogen. X-ray intensity data were collected at ALS beamline 5.0.1 and processed with XDS. The structure was solved by molecular replacement (Liebschner et al. 2019) using a single subunit of the $P3_121$ structure as a search model. Two solutions were obtained, consistent with the ASU being comprised of a DriD dimer. Both subunits contained bound ssDNA in the same location as observed in the $P3_121$ structure, but the 9mer was shared between the subunits due to packing, such that each subunit interacted with 4 bp of the ssDNA. See Supplemental Table S2 for data collection and refinement statistics.

Fluorescence polarization (FP) binding experiments

To measure ssDNA (5′-TAGTCTACT-3′ with a 5′fluorescein tag) binding to *C. crescentus* DriD proteins, increasing concentrations of each of the proteins were titrated into the sample cell containing 1 nM DNA in a buffer of 25 mM Tris (pH 7.5), 150 mM NaCl, and 5 mM $MgCl_2$. Samples were excited at 490 nm, and fluorescence emission was measured at 530 nm. RNA (5′-UAGUCUACU-3′ with a 5′ fluorescein tag) was similarly measured. Experiments measuring binding to the DriD operator dsDNA (top strand: 5′-ATACGACCGTTTCTGTCGCA-3′ with a 5′ fluorescein tag) were carried out with the WT FL DriD, DriD(73–327), and DriD mutants in the absence and presence of 1 mM nonfluoresceinated 9mer ssDNA (5′-TAGTCTACT-3′). All of the FP data were plotted using KaleidaGraph, and the curves were fit to deduce binding affinities. Notably, each purification had differing amounts of contaminating ssDNA; hence, technical repeats were performed. Three technical repeats were performed for each curve, and the standard errors from the three affinities were determined.

Size exclusion chromatography (SEC) analyses

SEC studies were carried out on FL DriD and FL DriD mixed at 1:1 molar ratio with ssDNA (5′-GAACTTGTAATTACAAGTTC-3′). The samples (at 2.7 mg/mL) were injected onto a Superdex S200 column (Fisher) with a mobile phase of 50 mM Tris (pH 7.5), 300 mM NaCl, and 5% (v/v) glycerol. The elution volumes of each sample were compared with a series of protein standards to determine the molecular weights. The standards used for calculation of the standard curve were 12.4 kDa of cytochrome c, 29.0 kDa of carbonic anhydrase, 66.0 kDa of albumin, 150.0 kDa of alcohol dehydrogenase, and 200 kDa of β-amylase.

β-Galactosidase assay

The indicated strains were grown up to mid-log (OD_{600} = 0.2–0.3) and treated with (or without) 15 µg/mL zeocin for 45 min. Harvested cells were permeabilized by adding 100 µL of chloroform to 900 µL of cells followed by vortexing. Cells were incubated for 15 min at 30°C prior to addition of ortho-nitrophenyl-β-galactoside. The assay and subsequent activity calculations were done as previously described (Miller 1972).

Data availability

ChIP-seq data are available at GEO accession number GSE197978. Coordinates and structure factor amplitudes have been deposited with the Protein Data Bank under the accession codes 7U02 and 7TZV.

Competing interest statement

The authors declare no competing interests.

Acknowledgments

This research was supported by National Institutes of Health (NIH) grants (R35GM130290 to M.A.S. and R01GM082899 to M.T.L.). M.T.L. is also an investigator of the Howard Hughes Medical Institute. We acknowledge beamlines 5.0.2 and 5.0.1 for X-ray diffraction data collection. The Advanced Light Source (ALS; Berkeley, CA) is a national user facility operated by Lawrence Berkeley National Laboratory on behalf of the US Department of Energy under contract DE-AC02-05CH11231, Office of Basic Energy Sciences. The Berkeley Center for Structural Biology is supported in part by the Howard Hughes Medical Institute. The ALS is a Department of Energy Office of Science user facility under contract DE-AC02-05CH11231. The Pilatus detector on 5.0.1. was funded under NIH grant S10OD021832. The ALS-ENABLE beamlines are supported in part by the NIH, National Institute of General Medical Sciences (grant P30 GM124169).

Author contributions: K.G., R.S., V.D.N., and M.A.S. performed experiments. M.A.S. and M.T.L. conceived and designed the experiments. K.G., M.A.S., and M.T.L performed analyses. M.A.S., K.G., and M.T.L wrote the paper.

References

Andis NM, Sausen CW, Alladin A, Bochman ML. 2018. The WYL domain of the PIF1 helicase from the thermophilic bacterium *Thermotoga elfii* is an accessory single-stranded DNA binding module. *Biochemistry* **57:** 1108–1118. doi:10.1021/acs.biochem.7b01233

Badrinarayanan A, Le TBK, Laub MT. 2015. Rapid pairing and resegregation of distant homologous loci enables double-strand break repair in bacteria. *J Cell Biol* **210:** 385–400. doi:10.1083/jcb.201505019

Bell JC, Kowalczykowski SC. 2016. RecA: regulation and mechanism of a molecular search engine. *Trends Biochem Sci* **41:** 491–507. doi:10.1016/j.tibs.2016.04.002

Chauhan A, Lofton H, Maloney E, Moore J, Fol M, Madiraju MVVS, Rajagopalan M. 2006. Interference of *Mycobacterium tuberculosis* cell division by Rv2719c, a cell wall hydrolase.

Mol Microbiol **62:** 132–147. doi:10.1111/j.1365-2958.2006.05333.x

da Rocha RP, Paquola AC, Marques Mdo V, Menck CFM, Galhardo RS. 2008. Characterization of the SOS regulon of *Caulobacter crescentus*. *J Bacteriol* **190:** 1209–1218. doi:10.1128/JB.01419-07

Doublié S. 1997. Preparation of selenomethionyl proteins for phase determination. *Methods Enzymol* **276:** 523–530. doi:10.1016/S0076-6879(97)76075-0

Dullaghan EM, Brooks PC, Davis EO. 2002. The role of multiple SOS boxes upstream of the *Mycobacterium tuberculosis lexA* gene—identification of a novel DNA-damage-inducible gene. *Microbiology* **148:** 3609–3615. doi:10.1099/00221287-148-11-3609

Ely B. 1991. Genetics of *Caulobacter crescentus*. *Methods Enzymol* **204:** 372–384. doi:10.1016/0076-6879(91)04019-K

Emsley P, Cowtan K. 2004. Coot: model-building tools for molecular graphics. *Acta Crystallogr D Biol Crystallogr* **60:** 2126–2132. doi:10.1107/S0907444904019158

Erill I, Campoy S, Barbé J. 2007. Aeons of distress: an evolutionary perspective on the bacterial SOS response. *FEMS Microbiol Rev* **31:** 637–656. doi:10.1111/j.1574-6976.2007.00082.x

Galhardo RS, Rocha RP, Marques MV, Menck CFM. 2005. An SOS-regulated operon involved in damage-inducible mutagenesis in *Caulobacter crescentus*. *Nucleic Acids Res* **33:** 2603–2614. doi:10.1093/nar/gki551

Galletto R, Amitani I, Baskin RJ, Kowalczykowski SC. 2006. Direct observation of individual RecA filaments assembling on single DNA molecules. *Nature* **443:** 875–878. doi:10.1038/nature05197

Guo MS, Haakonsen DL, Zeng W, Schumacher MA, Laub MT. 2018. A bacterial chromosome structuring protein binds overtwisted DNA to stimulate type II topoisomerases and enable DNA replication. *Cell* **175:** 583–597.e23. doi:10.1016/j.cell.2018.08.029

Guzzo M, Castro LK, Reisch CR, Guo MS, Laub MT. 2020. A CRISPR interference system for efficient and rapid gene knockdown in *Caulobacter crescentus*. *MBio* **11:** e02415-19. doi:10.1128/mBio.02415-19

Harper JW, Elledge SJ. 2007. The DNA damage response: ten years after. *Mol Cell* **28:** 739–745. doi:10.1016/j.molcel.2007.11.015

Hartwell LH, Weinert TA. 1989. Checkpoints: controls that ensure the order of cell cycle events. *Science* **246:** 629–634. doi:10.1126/science.2683079

Hill TM, Sharma B, Valjavec-Gratian M, Smith J. 1997. sfi-independent filamentation in *Escherichia coli* is *lexA* dependent and requires DNA damage for induction. *J Bacteriol* **179:** 1931–1939. doi:10.1128/jb.179.6.1931-1939.1997

Howe WE, Mount DW. 1975. Production of cells without deoxyribonucleic acid during thymidine starvation of lexA- cultures of *Escherichia coli* K-12. *J Bacteriol* **124:** 1113–1121. doi:10.1128/jb.124.3.1113-1121.1975

Huisman O, D'Ari R. 1981. An inducible DNA replication-cell division coupling mechanism in *E. coli*. *Nature* **290:** 797–799. doi:10.1038/290797a0

Huisman O, D'Ari R, George J. 1980. Inducible sfi dependent division inhibition in *Escherichia coli*. *Mol Gen Genet* **177:** 629–636. doi:10.1007/BF00272673

Jaffé A, D'Ari R, Norris V. 1986. SOS-independent coupling between DNA replication and cell division in *Escherichia coli*. *J Bacteriol* **165:** 66–71. doi:10.1128/jb.165.1.66-71.1986

Kabsch W. 2010. XDS. *Acta Crystallogr D Biol Crystallogr* **66:** 125–132. doi:10.1107/S0907444909047337

Kawai Y, Moriya S, Ogasawara N. 2003. Identification of a protein, YneA, responsible for cell division suppression during the SOS response in *Bacillus subtilis*. *Mol Microbiol* **47:** 1113–1122. doi:10.1046/j.1365-2958.2003.03360.x

Liebschner D, Afonine PV, Baker ML, Bunkoczi G, Chen VB, Croll TI, Hintze B, Hung LW, Jain S, McCoy AJ, et al. 2019. Macromolecular structure determination using X-rays, neutrons and electrons: recent developments in Phenix. *Acta Cryst* **D75:** 861–877. doi:10.1107/S2059798319011471

Little JW, Mount DW. 1982. The SOS regulatory system of *Escherichia coli*. *Cell* **29:** 11–22. doi:10.1016/0092-8674(82)90085-X

Little JW, Edmiston SH, Pacelli LZ, Mount DW. 1980. Cleavage of the *Escherichia coli lexA* protein by the *recA* protease. *Proc Natl Acad Sci* **77:** 3225–3229. doi:10.1073/pnas.77.6.3225

Liu G, Begg K, Geddes A, Donachie WD. 2001. Transcription of essential cell division genes is linked to chromosome replication in *Escherichia coli*. *Mol Microbiol* **40:** 909–916. doi:10.1046/j.1365-2958.2001.02434.x

Luyten YA, Hausman DE, Young JC, Doyle LA, Higashi KM, Ubilla-Rodriguez NC, Lambert AR, Arroyo CS, Forsberg KJ, Morgan RD, et al. 2022. Identification and characterization of the WYL BrxR protein and its gene as separable regulatory elements of a BREX phage restriction system. *Nucleic Acids Res* **50:** 5171–5190. doi:10.1093/nar/gkac311

Makarova KS, Anantharaman V, Grishin NV, Koonin EV, Aravind L. 2014. CARF and WYL domains: ligand-binding regulators of prokaryotic defense systems. *Front Genet* **30:** 10.3389.

Martins-Pinheiro M, Marques RCP, Menck CFM. 2007. Genome analysis of DNA repair genes in the α proteobacterium *Caulobacter crescentus*. *BMC Microbiol* **7:** 17. doi:10.1186/1471-2180-7-17

Miller J. 1972. *Experiments in molecular genetics*. Cold Spring Harb Lab Press, Cold Spring Harbor, NY.

Modell JW, Hopkins AC, Laub MT. 2011. A DNA damage checkpoint in *Caulobacter crescentus* inhibits cell division through a direct interaction with FtsW. *Genes Dev* **25:** 1328–1343. doi:10.1101/gad.2038911

Modell JW, Kambara TK, Perchuck BS, Laub MT. 2014. A DNA damage-induced, SOS-independent checkpoint regulates cell division in *Caulobacter crescentus*. *PloS Biol* **12:** e1001977. doi:10.1371/journal.pbio.1001977

Mukherjee A, Cao C, Lutkenhaus J. 1998. Inhibition of FtsZ polymerization by SulA, an inhibitor of septation in *Escherichia coli*. *Proc Natl Acad Sci* **95:** 2885–2890. doi:10.1073/pnas.95.6.2885

Müller AU, Imkamp F, Weber-Ban E. 2018. The mycobacterial LexA/RecA-independent DNA damage response is controlled by PafBC and the Pup-proteasome system. *Cell Rep* **23:** 3551–3564. doi:10.1016/j.celrep.2018.05.073

Müller AU, Leibundgut M, Ban N, Weber-Bad E. 2019. Structure and functional implications of WYL domain-containing bacterial DNA damage response regulator PafBC. *Nat Commun* **10:** 4653. doi:10.1038/s41467-019-12567-x

Müller AU, Kummer E, Schilling CM, Ban N, Weber-Ban E. 2021. Transcriptional control of mycobacterial DNA damage response by σ adaptation. *Sci Adv* **7:** eabl4064. doi:10.1126/sciadv.abl4064

Ogino H, Teramoto H, Inui M, Yukawa H. 2008. Divs, a novel SOS-inducible cell-division suppressor in *Corynebacterium glutamicum*. *Mol Microbiol* **67:** 597–608. doi:10.1111/j.1365-2958.2007.06069.x

Olivencia BF, Müller AU, Roschitzki B, Burger S, Weber-Ban E, Imkamp F. 2017. *Mycobacterium smegmatis* PafBC is involved in regulation of DNA damage response. *Sci Rep* **7:** 13987. doi:10.1038/s41598-017-14410-z

Opperman T, Murli S, Smith BT, Walker GC. 1999. A model for a *umuDC*-dependent prokaryotic DNA damage checkpoint. *Proc Natl Acad Sci* **96:** 9218–9223. doi:10.1073/pnas.96.16.9218

Phizicky EM, Roberts JW. 1981. Induction of SOS functions: regulation of proteolytic activity of *E. coli* RecA protein by interaction with DNA and nucleoside triphosphate. *Cell* **25:** 259–267. doi:10.1016/0092-8674(81)90251-8

Picton DM, Luyten YA, Morgan RD, Nelson A, Smith DL, Dryden DTF, Hinton JCD, Blower TR. 2021. The phage defence island of a multidrug resistant plasmid uses both BREX and type IV restriction for complementary protection from viruses. *Nucleic Acids Res* **49:** 11257–11273. doi:10.1093/nar/gkab906

Picton DM, Harling-Lee JD, Duffner SJ, Went SC, Morgan RD, Hinton JCD, Blower TR. 2022. A widespread family of WYL-domain transcriptional regulators co-localizes with diverse phage defence systems and islands. *Nucleic Acids Res* **2022:** gkac334. doi:10.1093/nar/gkac334

Symington LC. 2014. End resection at double-strand breaks: mechanism and regulation. *Cold Spring Harb Perspect Biol* **6:** a016436. doi:10.1101/cshperspect.a016436

Thanbichler M, Iniesta AA, Shapiro L. 2007. A comprehensive set of plasmids for vanillate- and xylose-inducible gene expression in *Caulobacter crescentus*. *Nucleic Acids Res* **35:** e137. doi:10.1093/nar/gkm818

Trusca D, Scott S, Thompson C, Bramhill D. 1998. Bacterial SOS checkpoint protein SulA inhibits polymerization of purified FtsZ cell division protein. *J Bacteriol* **180:** 3946–3953. doi:10.1128/JB.180.15.3946-3953.1998

Yan WX, Chong S, Zhang H, Makarova KS, Koonin EV, Cheng DR, Scott DA. 2018. Cas13d is a compact RNA-targeting type VI CRISPR effector positively modulated by a WYL-domain-containing accessory protein. *Mol Cell* **70:** 327–339.e5. doi:10.1016/j.molcel.2018.02.028

Zhang H, Dong C, Li L, Wasney GA, Min J. 2019. Structural insights into the modulatory role of the accessory protein WYL1 in the type VI-D CRISPR–Cas system. *Nucleic Acids Res* **47:** 5420–5428. doi:10.1093/nar/gkz269

Zhou B, Schrader JM, Kalogeraki VS, Abeliuk E, Dinh CB, Pham JQ, Cui ZZ, Dill DL, McAdams HH, Shapiro L. 2015. The global regulatory architecture of transcription during the *Caulobacter* cell cycle. *PLoS Genet* **11:** e1004831. doi:10.1371/journal.pgen.1004831